Organic & Biomolecular Chemistry

ROYAL SOCIETY OF CHEMISTRY

PAPER

View Article Online
View Journal | View Issue

Cite this: *Org. Biomol. Chem.*, 2020, **18**, 4090

The intermolecular anthracene-transfer in a regiospecific antipodal C_{60} difunctionalization†

Radu A. Talmazan, [a] Klaus R. Liedl, [a] Bernhard Kräutler [b] and Maren Podewitz *[a]

Ever since the discovery of fullerenes, their mono- and multi-functionalization by exohedral addition chemistry has been a fundamental topic. A few years ago, a topochemically controlled regiospecific difunctionalization of C_{60} fullerene by anthracene in the solid state was discovered. In the present work, we analyse the mechanism of this unique reaction, where an anthracene molecule is transferred from one C_{60} mono-adduct to another one, under exclusive formation of equal amounts of C_{60} and of the difficult to make, highly useful, antipodal C_{60} bis-adduct. Our herein disclosed dispersion corrected DFT studies show the anthracene transfer to take place in a synchronous retro Diels–Alder/Diels–Alder reaction: an anthracene molecule dissociates from one fullerene under formation of an intermediate, while undergoing stabilizing interactions with both neighbouring fullerene molecules, facilitating the reaction kinetically. In the intermediate, a planar anthracene molecule is sandwiched between two neighbouring fullerenes and forms equally strong 'double-decker' type π–π stacking interactions with both of these fullerenes. Analysis with the distortion interaction model shows that the anthracene unit of the intermediate is almost planar with minimal distortion. This analysis highlights the existence of simultaneous noncovalent interactions engaging both faces of a planar polyunsaturated ring and two convex fullerene surfaces in an unprecedented 'inverted sandwich' structure. Hence, it sheds light on new strategies to design functional fullerene based materials.

Received 11th March 2020,
Accepted 3rd May 2020

DOI: 10.1039/d0ob00520g

rsc.li/obc

Introduction

Fullerenes, the spherical molecular carbon allotropes first discovered in mass-spectrometric experiments in 1985,[1–3] open up exciting fields of chemical research.[4–7] The unique properties of the icosahedral C_{60} molecules have particularly inspired a multitude of studies concerning the functionalization of this polyunsaturated carbon compound by the means of addition reactions.[2,5,8] Early on, a range of cyclopropanations[4,8,9] and pyrrolidine forming reactions[8,10] as well as other formal cycloaddition reactions[8] were used very effectively. The synthetic interest in the chemistry of C_{60} was further boosted by its pronounced and theoretically rationalized selectivity for cycloaddition reactions at its so called [6,6]-bonds.[6,8,11–13] Indeed, the thermally reversible [4 + 2]-cycloaddition (Diels–Alder, DA) reaction has become a most versatile methodology for the creation of exohedrally functionalized fullerene derivatives.[8,14–17] Polycyclic aromatic hydrocarbons, such as anthracene,[8,17–21] other acenes,[22–25] and derivatives thereof,[26] were found to represent surprisingly suitable diene-components for functionalization of C_{60} by [4 + 2] cycloaddition reactions. The experimental work on the fullerene functionalization has been accompanied and guided by insightful theoretical studies.[27–30] Suitably functionalized fullerenes have been widely applied as key components,[31–34] in photovoltaic devices,[35–39] in artificial photosynthesis,[40,41] drug delivery,[32,42] bio- and nanomedicine,[41,42] in material science,[31,43–48] and as self-healing polymers.[49,50]

The molecular features of the fullerenes as polyunsaturated spherical carbon compounds have drawn particular attention to the synthesis of di- and multi-functionalized derivatives with high regio- and stereo-control.[8,51–57] Sequential addition reactions to create multi-adducts with exceptional architectures were presented,[57–63] including reactions between C_{60} and anthracenes, where mono-,[16–18,21,26,64] bis-,[19,64–68] and specific tris-adducts were reported.[63,69] The kinetic and thermodynamic driving forces for the formation of specific bis- and

[a]*Institute of General, Inorganic and Theoretical Chemistry, and Centre of Molecular Biosciences, University of Innsbruck, Innrain 80/82, 6020 Innsbruck, Austria. E-mail: maren.podewitz@uibk.ac.at*
[b]*Institute of Organic Chemistry, and Centre of Molecular Biosciences, University of Innsbruck, Innrain 80/82, 6020 Innsbruck, Austria*

†Electronic supplementary information (ESI) available: Detailed information about bis-adduct structures and energetics, comparison with experimental data, details on the distortion–interaction analyses, detailed energy decomposition analyses, structures of intermediates with smaller acenes, as well as *xyz* structure coordinates of all investigated species, their total energies and thermodynamic corrections. See DOI: 10.1039/d0ob00520g

tris-adducts has become a much discussed issue.[8] Thermolysis of the crystalline mono-adduct of C_{60} and anthracene has provided a strikingly efficient means for achieving regiospecific antipodal bis-addition.[65] The exquisite selectivity in this process was proposed to result from topochemical control in the solid state,[20,65] because the alternative solution chemistry led to a mixture of anthracene adducts, among them the antipodal bis-adduct as only a minor component.[19,70]

The (thermal) DA reaction has become a fundamental synthetic method for the stereo-controlled formation of two new C–C bonds in a 6-memberd ring structure, and a mechanistic textbook topic of (orbital and state) symmetry control,[71–74] thoroughly investigated in experimental and theoretical studies.[75–78] For typical hydrocarbons, the two new C–C bonds formed by the DA reaction are made in a concerted and thermally reversible process.[79–84] Quantum chemical studies have fully verified these 'basic rules' of the thermal [4 + 2]-cycloaddition chemistry.[85–90] The spherical architecture of the fullerenes induces pyramidalisation of the unsaturated carbon centers,[91] rendering the C_{60} electrophilic and specifically dienophilic – an early recognized factor for further enhancing reactivity in exohedral addition reactions,[8,28,92,93] decreasing the activation barrier in DA reactions.[94] Aromatic hydrocarbons first associate with C_{60} to form a non-covalently bound intermediate complex.[95] Recent studies at the example of benzene and C_{60} shed light on the interaction of a planar aromatic compound and a curved fullerene surface,[74] which was shown to be different in nature from π–π stacking interactions between two planes.

Regioselectivity of the DA cycloaddition with C_{60} has also been computationally investigated,[57,66,96–99] for example, revealing the preference of additions to the [6,6]-bond over the [5,6]-position to be attributed to more favourable interactions between the reactants in the transition state.[12] A finding later confirmed by decomposition of the electron activity[13] and also put forward by Garcia-Rodeja *et al.* to rationalize the regioselectivity of bis-cycloaddition reactions to fullerenes.[11]

The regiospecific formation of the antipodal bis-adduct from the crystalline mono-adduct of C_{60} and anthracene in the solid state suggested a topochemical control.[65] Potentially, the anthracene transfer between two pre-aligned mono-adducts, takes place in a synchronous fashion. However, the detailed reaction mechanism of this anthracene transfer was not established. Formally, this reaction could be achieved by a complete dissociation of the anthracene moiety from one mono-adduct by a retro-DA reaction, followed by the highly regio-selective DA-cycloaddition at another one. Alternatively, the anthracene transfer could proceed *via* a direct one-step reaction, where the transition state would represent a planar anthracene molecule interacting similarly with both fullerenes. A third variant could be *via* a synchronous two-step reaction, where in a retro-DA step an intermediate is first formed that is stabilized by two neighbouring fullerene moieties, followed by an addition at the back of the mono-adduct to generate the antipodal bis-adduct. Unravelling this reaction mechanism is of significant interest, as it implies a correlated defunctionalisation of one mono-adduct molecule, coupled with functionalization of a neighbouring mono-adduct molecule. Hence, a thorough computational analysis of this anthracene transfer between two fullerenes was carried out, in order to gain insights into the simultaneous interaction of two spherical and one planar polyunsaturated carbon molecules.

We investigated the topochemically controlled regiospecific anthracene transfer by two model reactions: reaction A describes the transfer of one anthracene molecule from one C_{60} fullerene mono-adduct to a 2nd C_{60} fullerene (Scheme 1, upper panel), while reaction B describes the transfer of one anthracene from one C_{60} fullerene mono-adduct to another C_{60} fullerene–anthracene mono-adduct, resulting in the antipodal bis-adduct (Scheme 1, lower panel). Density Functional Theory (DFT) calculations were performed to elucidate the reaction mechanism and to shed light on the interactions occurring at the unique reaction intermediate, where a planar anthracene is sandwiched between two fullerenes.

Computational methodology

As no high resolution X-ray crystal structures were available, the initial structures for the C_{60} fullerene and C_{60}:anthracene mono-adduct were set-up using Gaussview 4.1.2.[100] All subsequent structure optimizations and harmonic frequency cal-

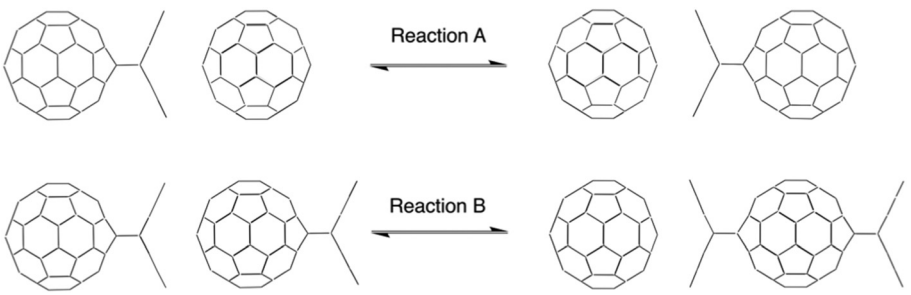

Scheme 1 Schematic representations of the investigated topochemically controlled anthracene transfer reactions. Reaction A depicts the transfer of one anthracene molecule from one C_{60}:anthracene mono-adduct to a C_{60} fullerene. Both the product and the educt represent identical structures. Reaction B depicts the anthracene transfer from one C_{60}:anthracene mono-adduct to another, resulting in the creation of one trans antipodal bis-adduct and one C_{60} fullerene.

culations were performed using Turbomole 7.3[101] and were done in C1 symmetry. Structure optimizations have been carried out with Density Functional Theory (DFT) utilizing the GGA density functional BP86[102–105] in combination with the def2-SVP basis set.[106] As shown in previous studies, empirical dispersion corrections, that are not intrinsically dealt with in DFT, are essential to obtain reliable structures in such extended π-systems and to localize reaction intermediates.[95] Therefore, Grimme's empirical dispersion corrections with Becke–Johnson damping of the DFT-D3[107] type were employed in all calculations. Selected structures were re-optimised with BP86/def2-TZVP[108]/D3 but structural differences were found to be small. Reported electronic energies were calculated as single points BP86/def2-TZVP/D3 on the BP86/def2-SVP/D3 optimized structures. An even larger def2-QZVP[109] basis set yielded very similar single point energies with differences less than 2 kJ mol^{-1} compared to def2-TZVP. Hence, the triple-zeta def2-TZVP basis set was considered to be accurate enough. To test the effect of the density functional, single point calculations with B3LYP[102,105,110,111]/def2-TZVP/D3 were computed on the BP86/def2-SVP/D3 optimized structures too. To validate our chosen methodology (density functional/basis set), we compared structural parameters with known experimental data. As to our knowledge, currently no crystal structure of the C_{60}:anthracene mono-adduct exists, we compared our calculated structures to the available experimental C_{60}:antracene bis-adducts ("edge" and "trans-4") structures.[67] Through the comparison with the aforementioned C_{60}:anthracene bis-adducts, it is shown that the methods chosen offer accurate structures, as the bond lengths deviate less than 0.01 Å from their crystal counterparts, while the angles and dihedrals are within 0.1°.

To further test our methodology, we also calculated the formation of the C_{60}:anthracene mono-adduct (see also Tables S6 and S7 in the ESI†), for which experimental data is available. In their 2004 paper, Sarova *et al.*[24] reported an activation enthalpy of $\Delta H^{\ddagger}$ = 57 kJ mol^{-1} and a Gibbs energy of $\Delta G^{\ddagger}$ = 93 kJ mol^{-1} in toluene. While this enthalpy is very close to our BP86 calculated value of $\Delta H^{\ddagger}$ = 59.4 kJ mol^{-1}, the Gibbs energy was with $\Delta G^{\ddagger}$ = 72.6 kJ mol^{-1} a bit underestimated. B3LYP values, however, overestimated the reaction barrier compared to experiment, $\Delta H^{\ddagger}_{\mathrm{B3LYP}}$ = 86.2 kJ mol^{-1} and $\Delta G^{\ddagger}_{\mathrm{B3LYP}}$ = 114.6 kJ mol^{-1}. The experimental reaction energy was found to be ΔH = −81 kJ mol^{-1} and ΔG = −23 kJ mol^{-1}. BP86 underestimated these values (ΔH = −54.5 kJ mol^{-1} and ΔG = 7.4 kJ mol^{-1}) and the trend got worse for B3LYP (ΔH = −31.4 kJ mol^{-1} and ΔG = 31.7 kJ mol^{-1}). Full optimisations and calculation of thermodynamic corrections at the BP86/D3/def2-TZVP level alleviated these shortcomings to some extend and correctly predicted the reaction to be exergonic with ΔG = −5.2 kJ mol^{-1} (see also Table S7†), but are not feasible given the size of the investigated structures. In our view, BP86 yielded a better overall performance although barriers are likely to be underestimated.

As the initial reaction is in solid-state, involving no charged species, no long-range interactions were expected. Indeed, taking the effect of the crystal environment into account by a dielectric constant, we chose ε = 4 here,[112] in agreement with previous studies, had little effect on the resulting energies. As can be seen from Table S5 in the ESI,† the electronic energies decreased by less than 2 kJ mol^{-1}. Thus, modelling the reaction in gas phase is adequate.

The correct stationary points were identified through harmonic frequency calculations, by examining the eigenvalues of the Hessian corresponding to each structure. Minima show only positive eigenvalues, while a transition state shows exactly one imaginary eigenvalue and its associated eigenvector corresponds to the reaction coordinate.

To obtain Gibbs energies, zero-point energies and thermal corrections at 298.15 K were calculated *via* approximation of the partition function by the standard rigid rotator and harmonic oscillator model using Turbomole's "freeh" tool. Obtained harmonic frequencies were scaled with a factor of 0.9914[113] to increase the accuracy. These corrections were calculated with BP86/def2-SVP/D3 and added to the BP86/def2-TZVP/D3 electronic energies.

Assuming (hindered) rotation of the nonfunctionalized C_{60} fullerene in **INT$_{\mathbf{Bis}}$**, **TS(INT$_{\mathbf{Bis}}$-3)** and **3**, results in additional contributions to the rotational entropy. To approximately account for these stabilizing effects, the structures were split up into two moieties – a C_{60} fullerene and a bis-adduct-like structure – and the rotational entropy was calculated for each moiety separately. The resulting contributions were summed up and replaced the rotational entropy contributions of the full complex in the Gibbs energy calculation, thereby, taking additional stabilizing effects due to the (hindered) rotation of the nonfunctionalized fullerene into account.

The 2D potential energy surfaces (PES) scans were obtained by modifying the structure along the chosen degrees of freedom, then subsequently calculating single point energies of each resulting structure. The resulting PES is visualized with Origin 2018b.[114]

To highlight the non-covalent interactions, NCIPLOT was used,[115] where the second eigenvalue of the electron-density Hessian matrix, sign(λ_2)ρ, is depicted on an isosurface of the reduced gradient s.[116] Areas with (weak) non-covalent interactions are characterized with a low (reduced) electron density gradient and a sign(λ_2)ρ close to zero (depicted in green). Large negative values of sign(λ_2)ρ are indicative of attractive interactions (depicted in blue), whereas large positive values of sign(λ_2)ρ indicate non-bonding repulsive interactions (depicted in red).

All structures were visualized using PyMol,[117] except for those depicting non-covalent interactions, which were displayed with VMD.[118]

Results

Mechanism of the topochemically controlled regiospecific C_{60} fullerene–anthracene transfer reaction

Prior to investigating the C_{60} fullerene–anthracene transfer reaction, we evaluated the reaction energies associated with

the formation of an isolated C_{60}:anthracene mono-adduct, see Scheme 2 (panel A), for which we found a stabilizing energy of $\Delta E = -62.4$ kJ mol^{-1} and $\Delta G = 7.4$ kJ mol^{-1}. Comparing this value to the experimentally found one of $\Delta G = -23$ kJ mol^{-1},[24] we see that the Gibbs energy is underestimated in our calculations (see also Computational methodology). However, the reaction is correctly predicted to be exergonic ($\Delta G = -5.2$ kJ mol^{-1}), when structures and thermodynamic corrections were calculated with a larger basis set (see also Table S7 in the ESI†). The formation of the complex **1** from the constituents yields an energy gain of $\Delta E = -123.7$ kJ mol^{-1} and $\Delta G = 3.2$ kJ mol^{-1} (see panel B). The coordination of a 2nd C_{60} fullerene to the C_{60}:anthracene mono-adduct to form **1**, exerts a stabilizing effect of $\Delta E = -60.1$ kJ mol^{-1} and a Gibbs reaction energy of $\Delta G = -4.2$ kJ mol^{-1} (panel C). Similarly, aligning two C_{60}:anthracene mono-adducts, to form the complex **2**, also results in a stabilization of $\Delta E = -58.5$ kJ mol^{-1} and $\Delta G = -7.8$ kJ mol^{-1}. It is noteworthy here that the stabilization energy of the second reaction partner to form the stable complexes **1** and **2**, is roughly the same as the formation energy of the C_{60}:mono-adduct, $-60.1/-58.5$ kJ mol^{-1} *vs.* -62.4 kJ mol^{-1}.

The proposed reaction pathway for the anthracene transfer as modelled by reaction A (see Scheme 1) is shown in Fig. 1, depicting educts, products, intermediates as well as transition states. Relative electronic energies (BP86/def2-TZVP/D3//BP86/def2-SVP/D3) are given in red and reaction Gibbs energies in green. For the sake of comparison, B3LYP/def2-TZVP/D3//BP86/def2-SVP/D3 are listed in blue.

While the formation of complex **1**, from two fullerenes and an anthracene molecule is energetically favoured, the most stable conformation of **1** was determined by a potential energy scan of the rotation of the 2nd fullerene as depicted in the ESI in Fig. S12.†

In the initial reaction step, complex **1** undergoes a Retro-Diels–Alder type process, in which the anthracene separates from the fullerene moiety, while still being trapped between and stabilized by the two fullerene species. The transition state **TS(1-INT$_{Mono}$)** for this reaction step has a barrier of $\Delta E^{\ddagger}$ = 79.4 kJ mol^{-1}, $\Delta G^{\ddagger}$ = 62.8 kJ mol^{-1} and $\Delta E^{\ddagger}_{B3LYP}$ = 94.7 kJ mol^{-1}. The reaction then proceeds to reach a stable intermediate structure (**INT$_{Mono}$**). This energy minimum structure is less stable than the educt, **1**, by ΔE = 21.8 kJ mol^{-1} (ΔG = 0.8 kJ mol^{-1}, and ΔE_{B3LYP} = 9.7 kJ mol^{-1}). Remarkably, the anthracene molecule lies completely flat between the two fullerenes, experiencing interactions with both sides. The reaction then continues in a mirrored fashion, with a [4 + 2] cycloaddition step. The second transition state, **TS(INT$_{Mono}$-1′)**, lies above the intermediate state, with $\Delta E^{\ddagger}$ = 57.6 kJ mol^{-1}, $\Delta G^{\ddagger}$ = 62.0 kJ mol^{-1}, and $\Delta E^{\ddagger}_{B3LYP}$ = 85.0 kJ mol^{-1}, exhibiting energy values identical to the reversed reaction to **TS(1-INT$_{Mono}$)**. The product compound (**1′**) is chemically identical to the educt **1** (ΔE = 0.0 kJ mol^{-1}). Compared to BP86, for B3LYP somewhat higher electronic energies were found. Nevertheless, both are in good agreement with each other.

In model reaction B (see Scheme 2), structure **2**, where two C_{60}:anthracene mono-adducts are aligned, reacts exclusively to the antipodal trans–bis-adduct in complex with C_{60} (denoted as **3**) undergoing a proposed mechanism as depicted in Fig. 2.

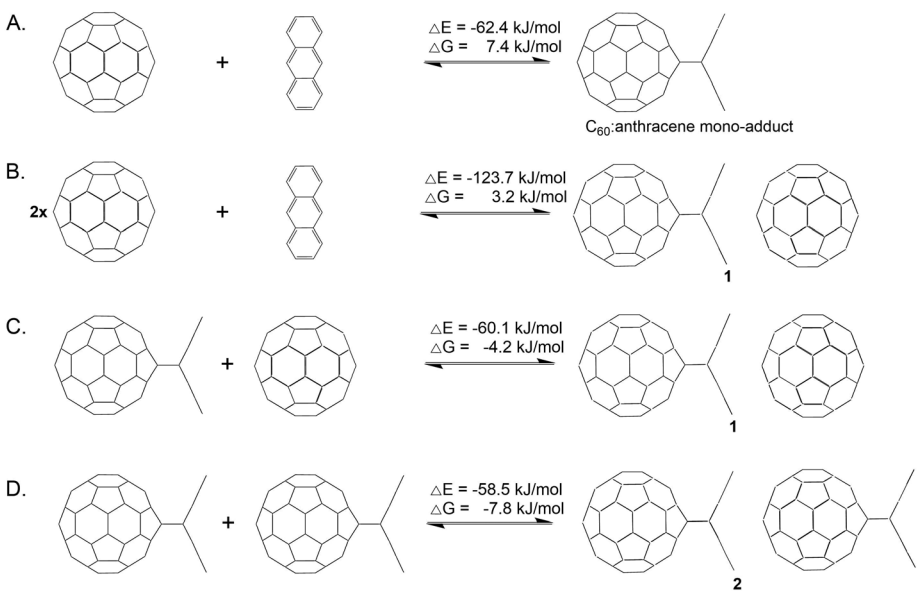

Scheme 2 Formation of the C_{60}:anthracene mono-adduct (A) from isolated C_{60} and anthracene, formation of complex **1** (B) from two isolated C_{60} molecules and anthracene, interaction of C_{60} with the C_{60}:anthracene mono-adduct to form complex **1** (C), interaction of two C_{60}:anthracene mono-adducts to form complex **2** (D). Relative Gibbs energies (ΔG) as well as relative electronic energies (ΔE) of the reactions are given in kJ mol^{-1} and were obtained with BP86/def2-TZVP/D3//BP86/def2-SVP/D3.

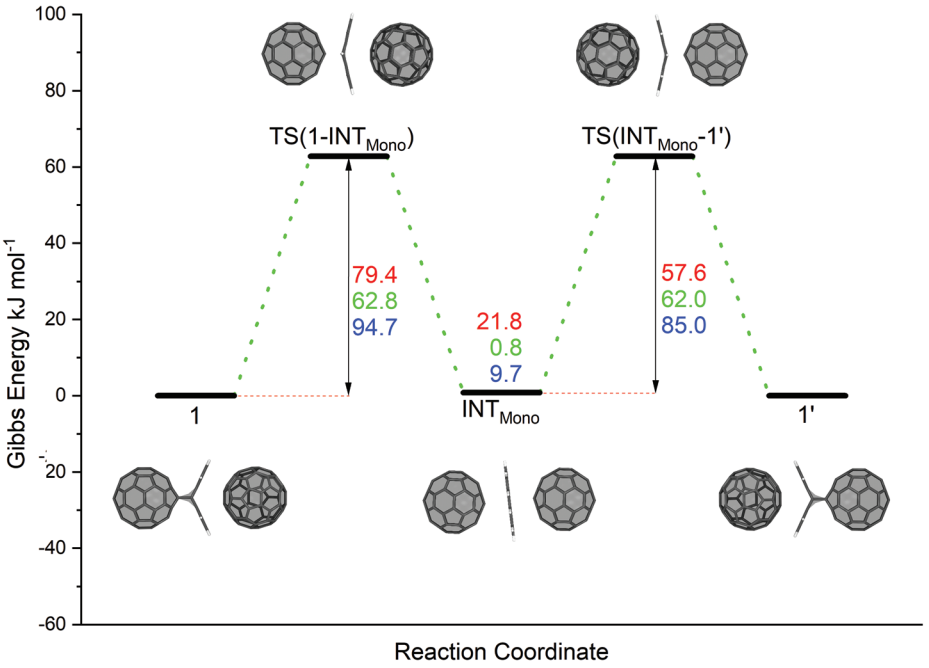

Fig. 1 Reaction mechanism of the anthracene transfer (reaction A in Scheme 1) from the C_{60}:anthracene mono-adduct (see complex **1**) to a neighbouring C_{60} fullerene (see complex **1'**) in a two-step synchronous Retro Diels–Alder and Diels–Alder reaction *via* an inverted sandwich intermediate (**INT$_{Mono}$**). Red values denote BP86/def2-TZVP/D3//BP86/def2-SVP/D3 relative electronic energies, green values denote reaction Gibbs energies and blue values denote relative electronic energies computed with B3LYP/def2-TZVP/D3//BP86/def2-SVP/D3. All values are in kJ mol^{-1}.

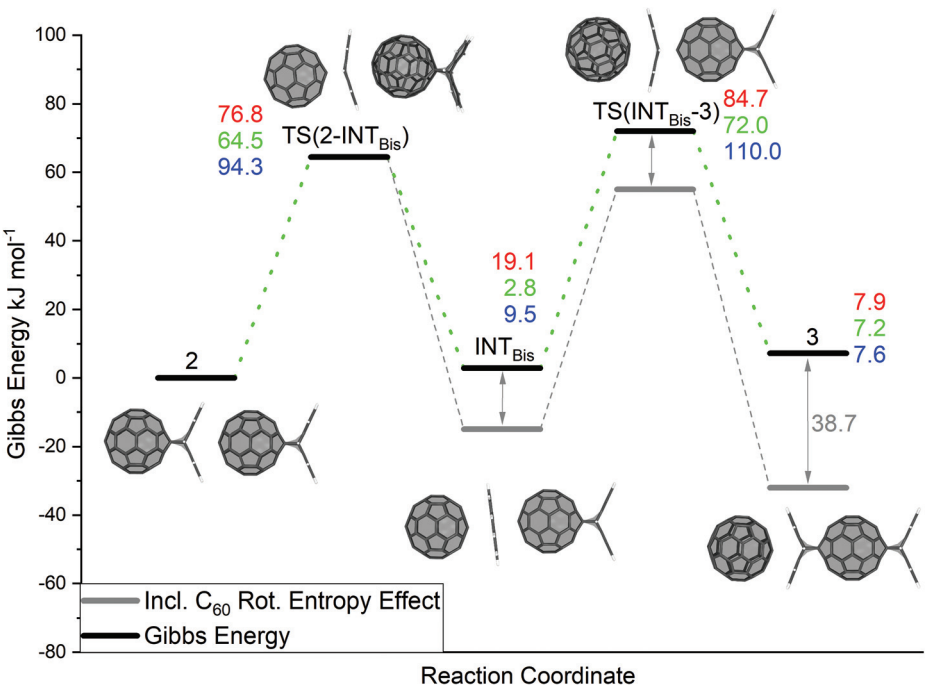

Fig. 2 Reaction pathway of the anthracene transfer between two mono-adducts (reaction B in Scheme 1). Electronic and the Gibbs energies of the reaction calculated with BP86/def2-TZVP/D3//BP86/def2-SVP/D3 are depicted in red and green, respectively. Energies calculated with B3LYP/def2-TZVP/D3//BP86/def2-SVP/D3 are shown in blue. The grey lines represent the Gibbs energy when additional rotational entropy of the C_{60} is taken into account too (see Computational methodology for details). All values are in kJ mol^{-1}.

Similar as in reaction A, the mechanism starts with a retro Diels Alder step to yield the stable intermediate **INT$_{Bis}$**, where the anthracene is trapped between two fullerenes. For this reaction step, an energy barrier of $\Delta E^{\ddagger}$ = 76.8 kJ mol^{-1} ($\Delta G^{\ddagger}$ = 64.5 kJ mol^{-1} and $\Delta E^{\ddagger}_{B3LYP}$ = 94.3 kJ mol^{-1}) was found, being very similar to the corresponding energy barrier in reaction A. The intermediate (**INT$_{Bis}$**) has a relative electronic energy ΔE = 19.1 kJ mol^{-1} (ΔE_{B3LYP} = 9.5 kJ mol^{-1}) and a Gibbs energy of ΔG = 2.8 kJ mol^{-1}, indicating the stabilizing effect of the neighbouring fullerenes on the anthracene. **INT$_{Bis}$** then reaches a 2nd transition state **TS(INT$_{Bis}$-3)** with a relative energy of $\Delta E^{\ddagger}$ = 84.7 kJ mol^{-1}, a relative Gibbs energy of $\Delta G^{\ddagger}$ = 72.0 kJ mol^{-1} ($\Delta E^{\ddagger}_{B3LYP}$ = 110.0 kJ mol^{-1}) before forming the antipodal bis-adduct in complex with C_{60}, denoted as **3**. The 2nd transition state is energetically less favourable than **TS(2-INT$_{Bis}$)**, but the barrier is with $\Delta E^{\ddagger}$ = 65.6 kJ mol^{-1} ($\Delta G^{\ddagger}$ = 69.2 kJ mol^{-1}, $\Delta E^{\ddagger}_{B3LYP}$ = 100.4 kJ mol^{-1}) slightly lower due to the higher energy of **INT$_{Bis}$**. In the initial calculations, the formed antipodal C_{60}:anthracenes bis-adduct in complex with C_{60} (**3**) is with a relative electronic energy of 7.9 kJ mol^{-1} (ΔG = 7.2 kJ mol^{-1} and ΔE_{B3LYP} = 7.6 kJ mol^{-1}) thermodynamically slightly less favoured than **2**. However, as shown by low barrier to rotation of the C_{60} moiety in complex **1** (see Fig. S12†), a hindered rotation of C_{60} in **INT$_{Bis}$**, **TS(INT$_{Bis}$-3)** and **3** could be anticipated resulting in additional rotational entropy. This contribution lowers the total Gibbs energy of **3** by about 39 kJ mol^{-1}, whereas a smaller stabilising effect is expected for **INT$_{Bis}$** and **TS(INT$_{Bis}$-3)** due to more pronounced rotational hindrance.

To further analyse the reaction, we used the distortion interaction model/activation strain model independently developed by Houk and Bickelhaupt[93,119,120] to characterise all stationary points in the reaction including intermediates and product/educt structures. As results are expected to be similar, we restrict our analyses to reaction A only.

We intended to quantify the effects of the deformations exerted by the weak, non-covalent interactions and to characterise the planar anthracene molecule in the intermediate structure. In our distortion interaction analysis along the reaction coordinate, the interactions on both sides of the anthracene were considered by taking the unperturbed fullerene and anthracene molecule as reference structures.

The deformation and interaction energies, $\Delta E_{Def.}$ and $\Delta E_{Int.}$, can be computed using the following equations,

$$\Delta E_{Electronic} = \sum \Delta E_{Def.} + \sum \Delta E_{Int.} \quad (1)$$

where $\Delta E_{Electronic}$ represents the electronic energy of the structure with reference to isolated C_{60} fullerene and anthracene molecules. The deformation energy $\Delta E_{Def.}$ can be defined as the energetic difference between the individual molecule fragments ($E_{Deformed}$) and their isolated, optimized structures ($E_{Optimized}$). In the case of reaction A, the molecule fragments are represented by two C_{60} fullerenes and one anthracene.

$$\Delta E_{Def.} = E_{Defomed} - E_{Optimized} \quad (2)$$

Table 1 Distortion–interaction energies for reaction A. $\Delta E_{C_{60}\ Def.}$ represents the deformation energy of the two fullerenes; $\Delta E_{Anthracene\ Def.}$ represents the deformation energy of the anthracene; $\Delta E_{Total\ Def.}$ represents the sum of all deformation energies; $\Delta E_{Total\ Int.}$ represents the total interaction energy; $\Delta E_{Electronic}$ represents the electronic energy of the structure (for details see eqn (1–3))

Structure	**1**	**TS(1-INT$_{Mono}$)**	**INT$_{Mono}$**	**TS(INT$_{Mono}$-1′)**	**1′**
$\Delta E_{C_{60}\ Def.}$	174.3	48.4	18.5	48.4	174.3
$\Delta E_{Anthracene\ Def.}$	306.8	86.0	3.2	86.0	306.8
$\Delta E_{Total\ Def.}$	481.1	134.4	21.7	134.4	481.1
$\Delta E_{Total\ Int.}$	−583.6	−157.6	−102.4	−157.6	−583.6
$\Delta E_{Electronic}$	−102.5	−23.1	−80.7	−23.1	−102.5

By summing up the deformation energies $\Delta E_{Def.}$ and subtracting them from the electronic energy $\Delta E_{Electronic}$, we obtain the total interaction energy as

$$\sum \Delta E_{Int.} = \Delta E_{Electronic} - \sum \Delta E_{Def.} \quad (3)$$

When looking at the deformation energies $\Delta E_{Electronic}$ for the C_{60} fullerene along the reaction coordinate of reaction A as listed in Table 1, a maximum of $\Delta E_{C_{60}\ Def.}$ = 174.3 kJ mol^{-1} was found in **1** and **1′**, decreasing to 48.4 kJ mol^{-1} in the transition states and reaching a minimum in the intermediate **INT$_{Mono}$**. A mere deformation of $\Delta E_{C_{60}\ Def.}$ = 18.5 kJ mol^{-1} indicate that the structure is close to that of an unperturbed C_{60} fullerene. The same trend was observed for the deformation of anthracene. Of course, the strong deformations of bound anthracene are alleviated upon reaching the TS. However remarkably, **INT$_{Mono}$** has a very small anthracene deformation energy of only $\Delta E_{Anthracene\ Def.}$ = 3.2 kJ mol^{-1}, indicating that the anthracene is stabilized almost at its ideal gas phase geometry. The total deformation energy is, therefore, by far the smallest in **INT$_{Mono}$** ($\Delta E_{Total\ Def.}$ = 21.7 kJ mol^{-1}). The interplay of distortion and interaction results in a striking stabilization of **INT$_{Mono}$** in unprecedented 'inverted sandwich' structure with $\Delta E_{Electronic}$ = −80.7 kJ mol^{-1}, when assembled from two fullerenes and an anthracene.

Structure and electronic properties of the intermediate INT$_{Mono}$

To shed light on the nature of the unprecedented intermediates, **INT$_{Mono}$** and **INT$_{Bis}$**, where the anthracene lies almost perfectly planar between the two curved fullerenes, potential energy surfaces as well as non-covalent interactions were investigated.

Two 2D potential energy surface (PES) scans were performed at the example of **INT$_{Mono}$**, see Fig. 3. On the left-hand side (A), the PES for the displacement of the left C_{60} fullerene along the *y*-axis and its rotation around the *x*-axis is depicted. On the right-hand side (B), the rotation of the anthracene around the *x*-axis and its tilt, *i.e.*, its rotation around the *z*-axis is shown. As evident from the plot, the PES is rather flat allowing for a wide range of motion of the anthracene and fullerene without significant increase in

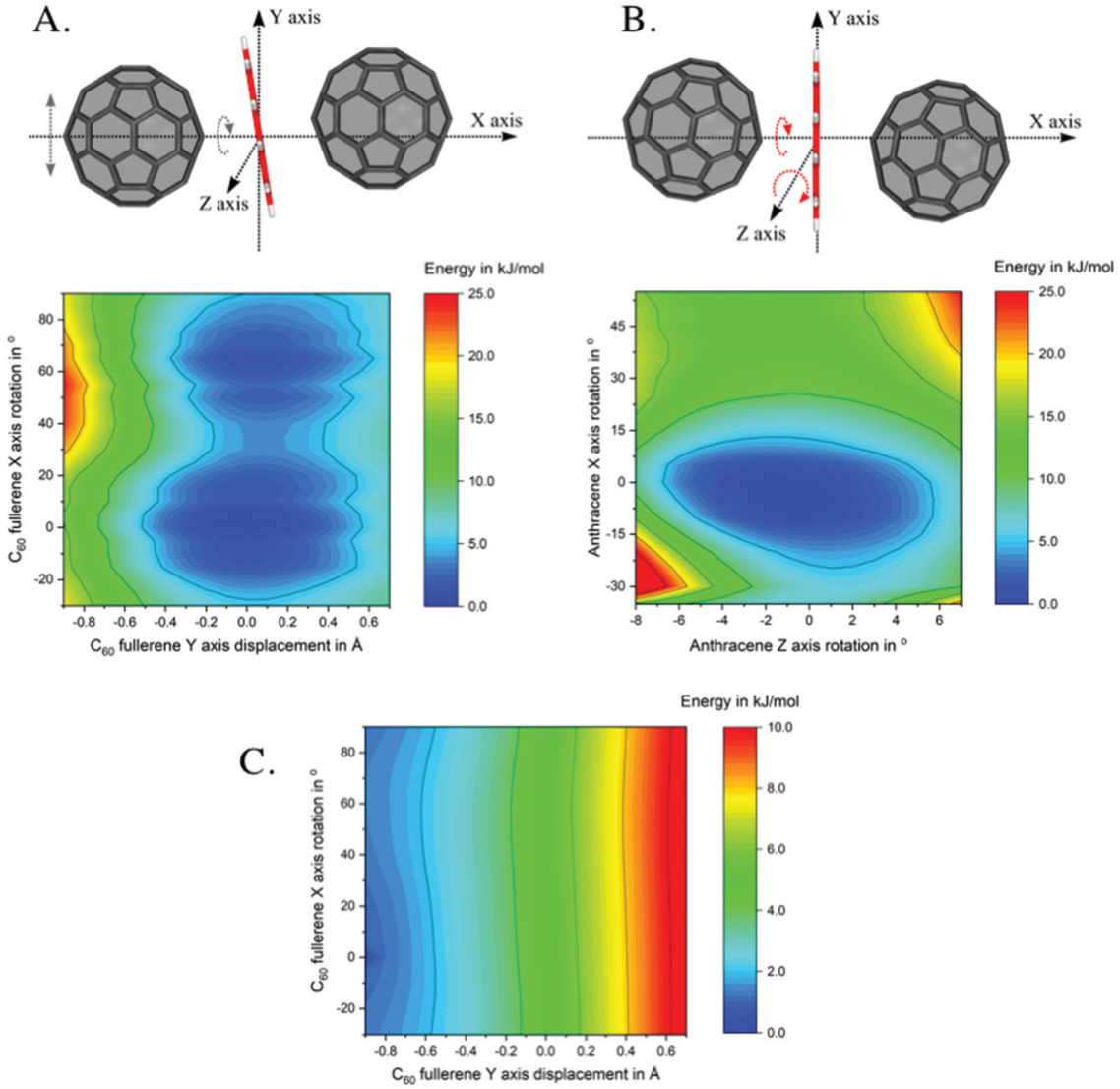

Fig. 3 2D potential energy surfaces scans of the intermediate $\mathbf{INT_{Mono}}$. A. The C_{60} is rotated around the *x*-axis by −30° and +90° and displaced along the *y*-axis by +0.9 and −0.7 Å relative to the geometry of the $\mathbf{INT_{Mono}}$, as indicated by grey arrows. B. Anthracene is rotated along the *x*-axis by −40° and +55° and the *z*-axis by −8° and +7° from $\mathbf{INT_{Mono}}$, as indicated by red arrows; C. relative empirical dispersion corrections for the PES scan depicted in A. Displayed energies are given in kJ mol^{-1}, calculated with BP86/def2-SVP/D3.

energy. The energy minimum, as verified by analysis of the harmonic frequencies, was determined for a conformation, where – compared to an idealized C_{2v} symmetric complex – the anthracene is rotated by 32.5° around the *x*-axis and rotated around the *z*-axis by 8° resulting in a tilt. Last, the two fullerenes are oriented with their centre of mass above and below the *xz*-plane (see Fig. 3). Consequently, this anthracene orientation maximizes attractive interactions with the neighbouring fullerenes. While the dispersion corrections become more favourable when the anthracene–fullerene distance is minimized (see *x*-axis in the dispersion energy surface shown in Fig. 3C), it can also be seen that these interactions depend on the rotation of the fullerene (see *y*-axis in Fig. 3C).

We also tested replacement of anthracene by smaller rings, such as naphthalene and benzene, in $\mathbf{INT_{Mono}}$. Both naphthalene and benzene assume positions very close to that of the anthracene, being tilted by 8° (rotated by 8° around the *z*-axis) and rotated by 32.5° around the *x*-axis, even though the arrangement of the acene over the ring slightly differs (see Fig. S15 ESI†).

To further elucidate the interactions between the anthracene and their two neighbouring fullerenes, the non-covalent interactions were visualized using NCIPLOT[115,116] as depicted in Fig. 4. Here, the electronic density is examined as a function of an isosurface of the reduced gradient, thus allowing for a quantitative assessment of these interactions. Red areas in Fig. 4 denote strong repulsive interaction, whereas green

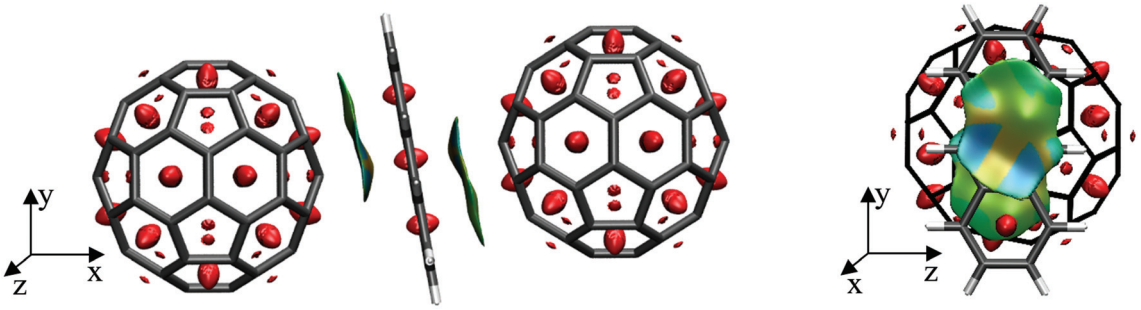

Fig. 4 Interactions between the C_{60} fullerenes and the anthracene molecule in the INT_{mono} structure, plotted as an isosurface of the reduced density gradient *s*. Left: Side view of INT_{mono}; Right: transversal view of INT_{Mono}. An isosurface of s = 0.3 a.u. is depicted and the colours from blue to red correspond to sign(λ_2)ρ, values from −0.1 to 0.1 a.u.

denote weakly attractive regions, typical for dispersive interactions. These are found between the upper and middle C_6-ring of anthracene and the closest C_6-ring of the left fullerene as well as between the middle and lower C_6-ring of anthracene and the closest C_6-ring of the right fullerene, showing symmetric π–π double decker interactions in this 'inverted sandwich' structure.

Characterization of transition states

To evaluate the effect of a second fullerene or C_{60}:anthracene on the transition state for the cycloaddition or cycloreversion, we analysed the structural and electronic effects in the obtained transition states **TS(INT_{Bis}-3)**, **TS(2-INT_{Bis})**, and **TS(1-INT_{Mono})** and compared them to a number of C_{60}:arene transition states as well as the C_{60}:butadiene transition state (Table 2).

Most notable differences in the transition states can be seen in the C1–C10′ and C9–C9′ bond lengths. With $TS_{Butadiene}$ being a somewhat different case due to the absence of an aromatic ring, it can be seen the C1–C10′ and the C9–C9′ bond lengths increase with increasing ring size and further increases in the presence of a 2nd fullerene. In addition, the transition states become more asymmetric in **TS(1-INT_{Mono})**, **TS(2-INT_{Bis})** and **TS(INT_{Bis}-3)**. As the TS of the mono-adduct and of the antipodal bis-adduct (see ESI Fig. S7†) are almost perfectly symmetric, the asymmetry likely arises due to interaction with the 2nd fullerene, which is aligned slightly off axis.

Considering the energy barriers, when the non-covalently bound intermediate is taken as a reference (see Fig. S16† for structures), it can be seen that **TS(1-INT_{Mono})** and **TS(2-INT_{Bis})** not only have very similar barrier heights but also the lowest energy barriers for this set of structures (57.6 and 57.7 kJ mol^{-1}). The formation of the bis-adduct in **TS(INT_{Bis}-3)** has a higher energy barrier with $\Delta E^{\ddagger}_{Barrier}$ = 65.6 kJ mol^{-1} as expected, which is very similar to that of the antipodal bis-adduct (67.2 kJ mol^{-1}, see ESI Table S2†), slightly surpassing the activation energy necessitated by the formation of the C_{60}:anthracene mono-adduct at $\Delta E^{\ddagger}_{Barrier}$ = 62.4 kJ mol^{-1}. The energy barrier for the formation of mono-adducts increases as the diene gets smaller, $\Delta E^{\ddagger}_{Barrier}$ = 100.9 kJ mol^{-1} for $TS_{Naphtalene}$, $\Delta E^{\ddagger}_{Barrier}$ = 128.1 kJ mol^{-1} for $TS_{Benzene}$, with the notable exception of $TS_{Butadiene}$, where the energy is the lowest out of all investigated transition states, at only 30.5 kJ mol^{-1}.

We also performed a distortion–interaction analysis[93,119,120] on the transition states depicted in Fig. 5, for details see illustration in Fig. S13 in the ESI.† It can be seen from Table 3, that the total deformation energies are smallest, 115.9 and

Table 2 Relevant structural parameters of different transition states involved in C_{60} functionalization. Distances are given in Å, angles, and dihedral angles in °. $\Delta E^{\ddagger}_{Barrier}$ represents the energy barrier between the non-covalently bound intermediate (see Fig. S16† for structures) and their respective transition state in kJ mol^{-1} calculated as single points (BP86/def2-TZVP/D3) on the fully optimized BP86/def2-SVP/D3 structures

Structure	TS(INT_{Bis}-3)	TS(2-INT_{Bis})	TS(1-INT_{Mono})	$TS_{Monoadduct}$	$TS_{Naphtalene}$	$TS_{Benzene}$	$TS_{Butadiene}$
Bond lengths							
C1–C10′	2.180	2.185	2.184	2.156	2.097	2.014	2.883
C9–C9′	2.155	2.170	2.172	2.156	2.043	2.014	2.884
C1–C5	1.485	1.483	1.484	1.485	1.493	1.497	1.479
C1–C9	1.480	1.482	1.482	1.483	1.482	1.481	1.480
Angles							
C5–C1–C2	104.5	104.7	104.7	104.5	103.7	103.4	105.3
C5–C1–C9	117.6	117.8	117.7	117.6	116.8	117.0	118.3
Dihedral angles							
C5–C1–C9–C10	126.8	126.8	126.9	126.2	124.5	123.4	129.0
C10′a–C10′–C9′–C9′a	147.8	147.8	148.4	148.6	144.9	143.0	—
$\Delta E^{\ddagger}_{Barrier}$	65.6	57.7	57.6	62.4	100.9	128.1	30.5

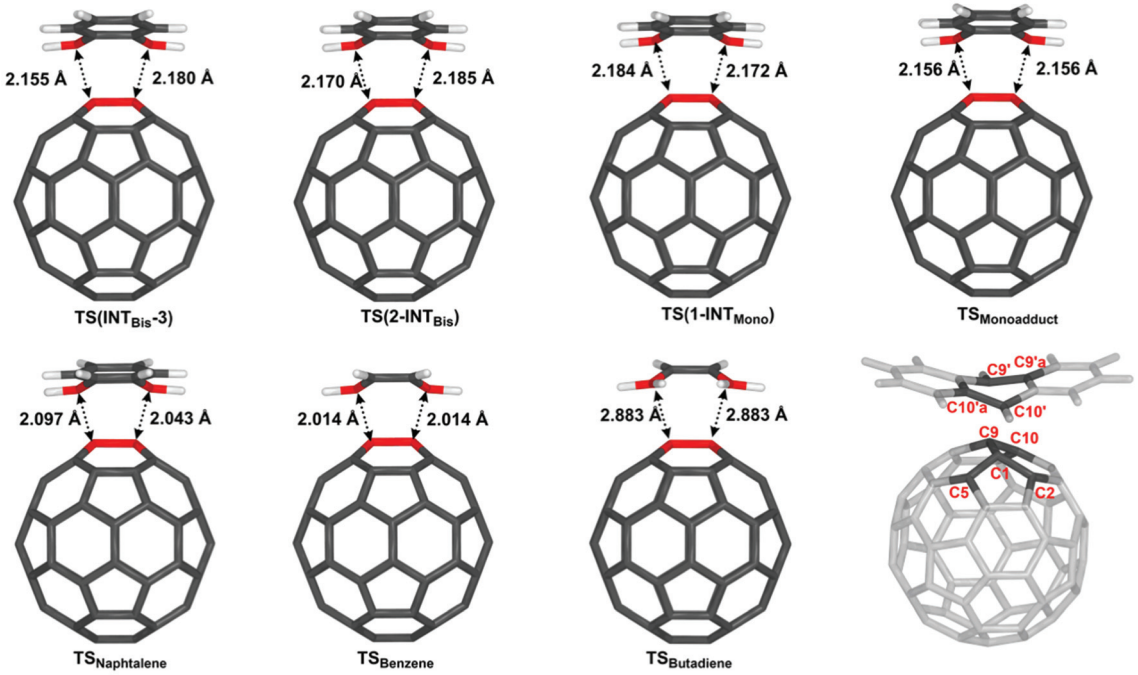

Fig. 5 Comparison of various transition state structures: **TS(INT$_{Bis}$-3)**, **TS(2-INT$_{Bis}$)**, and **TS(1-INT$_{Mono}$)** as previously discussed; **TS$_{Monoadduct}$** denotes the TS to the formation of the C_{60}:anthracene mono-adduct, **TS$_{Naphtalene}$** and **TS$_{Benzene}$** denote the TS to the formation of the C_{60}:naphthalene and C_{60}:benzene mono-adducts, whereas **TS$_{Butadiene}$** denotes the TS for the reaction of butadiene with C_{60}. Numbering of structures according to IUPAC. Structures were fully optimized with BP86/def2-SVP/D3. To enhance the readability, the anthracene, naphthalene, and benzene structures have been truncated and show only part of the aromatic ring structure.

Table 3 Distortion–interaction energies for the transition states depicted in Fig. 5. $\Delta E_{C_{60}\ Def.}$ represents the deformation energy of the fullerene and C_{60}:anthracene mono-adduct, respectively, when compared with its geometry in the corresponding non-covalently bound intermediate; $\Delta E_{Diene\ Def.}$ represents the total energy difference of the diene, when compared with the corresponding geometry in the intermediate; $\Delta E_{Total\ Def.}$ represents the sum of all deformation energies; $\Delta E_{Total\ Int.}$ represents the difference between the barrier energy and the total deformation; $\Delta E_{Barrier}$ represents the electronic energy difference between the transition state and the corresponding intermediate

Structure	TS(INT$_{Bis}$-3)	TS(2-INT$_{Bis}$)	TS(1-INT$_{Mono}$)	TS$_{Monoadduct}$	TS$_{Naphtalene}$	TS$_{Benzene}$	TS$_{Butadiene}$
$\Delta E_{C_{60}\ Def.}$	32.8	32.5	30.8	34.9	45.2	53.3	17.6
$\Delta E_{Diene\ Def.}$	85.2	83.5	82.8	84.3	114.0	133.4	50.1
$\Delta E_{Total\ Def.}$	118.0	115.9	113.6	119.2	159.2	186.6	67.7
$\Delta E_{Total\ Int.}$	−52.4	−58.3	−56.0	−56.8	−58.3	−58.3	−37.2
$\Delta E^{\ddagger}_{Barrier}$	65.6	57.7	57.6	62.4	100.9	128.3	30.5

113.6 kJ mol^{-1}, for the two transition states **TS(2-INT$_{Bis}$)** and **TS(1-INT$_{Mono}$)**, where a C_{60}:anthracene mono-adduct is formed in the presence of a second fullerene. The deformation energy increases slightly when we look at the mono-adduct, at 119.2 kJ mol^{-1} as well as when reducing the size of the added molecule. Thus, it reaches 159.2 kJ mol^{-1} for naphthalene and 186.6 kJ mol^{-1} for benzene. Butadiene, requires a minimal amount of deformation energy compared to the other transition states, with a total of 67.7 kJ mol^{-1}. The interaction energy of the transfer reactions is consistent with all transition states involving aromatic hydrocarbons showing little variation. **TS(INT$_{Bis}$-3)** has the least favourable energy, −52.4 kJ mol^{-1}, and **TS(2-INT$_{Bis}$)** the most favourable one, at −58.3 kJ mol^{-1}. The deformation energy largely correlates with the barrier height with the exception of **TS(INT$_{Bis}$-3)**, where the less favourable interaction energy and higher C_{60} deformation energy can be considered the cause for the high transition-state energy.

Discussion

Reaction mechanism

Both investigated reaction A and B (see Scheme 1) follow a synchronous two-step retro DA/DA sequence, where the anthracene dissociates while still being trapped between two fullerenes during the entire reaction to yield a regiospecific difunctionalization.

The starting point of reaction A is represented by a stabilized complex, **1**, consisting of a C_{60} fullerene and a C_{60}:anthracene mono-adduct. The interactions between the mono-adduct and the fullerene, while being favourable, allow for a large rotational movement of the C_{60} fullerene as the potential energy surface is very shallow (see Fig. S12†). This indicates that a pre-alignment in the first reaction step is not immanent to the structures, but facilitated due to the confined arrangement of molecules in the solid state.

By comparing the transition states of reactions A and B, with several transition states for C_{60}:arene-mono-adduct formation a systematic trend becomes apparent: in the series from benzene, to naphthalene, to anthracene, to **TS(1-INT$_{Mono}$)**, to **TS(2-INT$_{Bis}$)**, and to ,**TS(INT$_{Bis}$-3)** the C1–C10′ and C9–C9′ bonds elongate, which relates well to the Hammond postulate. The cycloaddition becomes more exothermic (compare Table S9†), making the TS more intermediate like (earlier TS for cycloaddition/later TS for cycloreversion). Moreover, the 2nd fullerene induced a difference in the two bond lengths resulting in more asymmetric transition states, which likely arises because the 2nd fullerene is located off centre the anthracene–fullerene axis, but whether this is a result of the gas phase calculation and whether this also pertains the solid state remains speculative. Still, the presence of the 2nd fullerene decreases the transition-barrier height mostly by minimizing deformation.

Energetics. The transition states **TS(1-INT$_{Mono}$)** and **TS(INT$_{Mono}$-1′)** are mirror images of each other with an energy barriers of $\Delta G^{\ddagger}$ = ~60 kJ mol^{-1}. In agreement with other studies on mono-adducts, these are concerted transition states as indicated by their symmetric structures.[95] Finding identical barriers for both the retro Diels–Alder reaction to form the intermediate **INT$_{Mono}$** and the Diels–Alder reaction to form **1′**, is in contrast to experimental and theoretical studies of the C_{60}:anthracene mono-adduct formation, where the retro Diels–Alder reaction is found to have a significantly higher barrier[24,95] emphasizing once more the effect of the 2nd fullerene.

The reaction rate for the elementary cycloreversion step and the according half-life can be calculated using the Eyring equation,

$$k = \frac{\kappa k_B \cdot T}{h} \cdot e^{-\frac{\Delta G^{\ddagger}}{RT}} \quad (4)$$

$$t_{1/2} = \frac{\ln 2}{k} \quad (5)$$

where k is the reaction rate, κ is the transmission coefficient, here equal to one, k_B is the Boltzmann constant, h the Planck constant, $\Delta G^{\ddagger}$ the Gibbs energy barrier, R the gas constant, and T the temperature in Kelvin.

At room temperature, for reaction A reaction rate of 6.2 × 10^{1} s^{-1} is obtained for the cycloreversion ($t_{1/2}$ = 1.1 × 10^{-5} s), while heated up to 180 °C the reaction rate increases to k = 5.4 × 10^{5} s^{-1} ($t_{1/2}$ = 1.3 × 10^{-9} s). Similar values are found for reaction B, k = 4.8 s^{-1} ($t_{1/2}$ = 1.5 × 10^{-1} s) at room temperature and k = 1.0 × 10^{5} s^{-1} ($t_{1/2}$ = 6.9 × 10^{-9} s) at 180 °C. This agrees with the experimentally observed fast reaction at elevated temperatures and shows that the reaction model is indeed plausible.[65] It should be kept in mind, however, that reported calculated values for the energy barriers might be underestimated by several kJ mol^{-1} (see also Computational methodology and Tables S5–S7 in the ESI†).

Concerning reaction B, our initial calculations showed structure **3** is slightly less table than the educts. However, thermodynamic corrections are calculated with the standard rigid rotator model/harmonic oscillator model of the entire complex **3**. In this model, the rotational entropy is calculated for the whole complex not allowing for individual rotation of the C_{60} fullerene.

If we assume the nonfunctionalized C_{60} fullerene to be rotating, the additional rotational entropy lowers ΔG of **INT$_{Bis}$**, **TS(INT$_{Bis}$-3)**, and **3**. In the limit of a freely rotating C_{60}, the Gibbs energy of **3** is lowered by approximately 39 kJ mol^{-1} making it the thermodynamically favoured species. The gain in rotational entropy for **INT$_{Bis}$** and **TS(INT$_{Bis}$-3)** can be expected to be smaller as the C_{60} rotation is potentially more hindered there, hence, we have not assigned any number in Fig. 2, but just indicated the stabilising effect. In any case, this correction to the standard model makes **3** the thermodynamically favoured product of reaction B and entropic effects are likely to be the driving force for this reaction.[65] Of course, this also holds for reaction A, but the effect is symmetric and does not affect the relative energy difference between the structures.

Regiospecificity. In the experimental solid-state reaction, exclusively the formation of the antipodal bis-adduct and free C_{60} fullerene was observed, a surprising, much commented and further explored process.[65,96,121–123] However, when comparing all possible bis-adducts as listed in Table S3 in the ESI,† the antipodal bis-adduct, is the least stable adduct. In addition, it also has the highest activation energy of 67.2 kJ mol^{-1} of all bis-adducts. Thus, in the absence of a 2nd fullerene, the antipodal bis-adduct would not be thermodynamically favoured. This provides strong evidence that a prealignment of C_{60}:anthracene monomers in the crystal structure and a synchronous coupled retro DA/DA reaction facilitates the observed topochemically controlled regiospecific antipodal difunctionalization.

The planar intermediate INT$_{Mono}$ with double decker π–π stacking interactions

INT$_{Mono}$ represents an unprecedented case of non-covalent π–π-stacking interactions between a planar and two curved surfaces.

Being exposed to a convex surface, planar structures such as anthracene tend to deform and adapt to the convex shape to maximize attractive dispersive interactions as indicated by the slight bend in the anthracene when forming a noncovalently bound intermediate with C_{60} as depicted in Fig. S17.† The deformation of the anthracene can be characterized by the bowl depth – calculated according to ref. 124, which amounts

to 0.14 Å for the C_{60} and anthracene intermediate. Such a deformation is also observed for other acenes.[95] In the presence of a 2nd C_{60} fullerene as in **INT$_{Mono}$** and **INT$_{Bis}$**, the anthracene is almost perfectly planar with minimal distortion from the gas phase geometry. This finding is supported by the distortion–interaction analysis, where for **INT$_{Mono}$** a minimal distortion of anthracene was found (3.2 kJ mol^{-1}). Thus, an alignment with the two fullerenes stabilizes a planar structure and counteracts the tendency of a large aromatic hydrocarbons to slightly bend towards C_{60} surfaces.

Further analysing the interactions between the C_{60}:anthracene and the 2nd fullerene (**1**, **TS(1-INT$_{Mono}$)**, **INT$_{Mono}$**), we see that the calculated the bowl depth[124] of anthracene correlates with the stabilization energy: **INT$_{Mono}$** (anthracene is planar) has the smallest stabilization energy (−51.9 kJ mol^{-1}) but it gets more favourable for **TS(1-INT$_{Mono}$)**, with a bowl depths of anthracene of 0.88 Å and an interaction energy of −57.8 kJ mol^{-1}. The stabilization energy is with −60.1 kJ mol^{-1} most pronounced in **1**, where a bowl depth of 1.63 Å was determined. This finding is in line with previous studies, where the bowl depth of hexabenzocorones was found to correlate with the C_{60} interaction strength, reaching an optimum at 1.5 Å.[124]

Concerning the position of the anthracene relative to the two fullerenes, a rotation around the *x*-axis by 32.5° and a rotation around the *z*-axis by 8° with respect to an idealized C_{2v} symmetric molecule maximizes favourable interactions. This orientation is very different from the position an anthracene molecule adopts when interacting with a single C_{60} fullerene, where it is aligned directly on top of the bond-to-be-formed, along the common edge formed by two C6 rings on the fullerene.[95,125] When a second fullerene is added, the simultaneous double decker π–π stacking interactions induce a rearranging of the anthracene to stack the 6-membered carbon ring of one C_{60} on its upper ring and of the other C_{60} fullerene on the lower ring. In contrast, if two benzene molecules are stacked in parallel, the two rings are slightly shifted so that one carbon atom stands over the centre of the second benzene molecule.[126] In addition, the presented intermediate **INT$_{Mono}$** shows with 3.06 Å shorter π–π stacking distances between anthracene and each fullerene (compare also with ref. 127) than found in planar π–π stacking structures. For example, in benzene dimers the distance between the two faces is 3.8 Å.[126]

Conclusion

Our quantum chemical investigations revealed the anthracene-transfer in the experimentally observed regiospecific C_{60}:anthracene difunctionalization to proceeds *via* a synchronous two-step retro Diels–Alder/Diels Alder type process. The central species is a low lying intermediate, where a planar anthracene molecule is non-covalently bound to two fullerene moieties. The rate determining step in this reaction is the initial cycloreversion to form anthracene sandwiched intermediates, either in the form of **INT$_{Mono}$** or as **INT$_{Bis}$**. The presence of the second fullerene lowers the activation energies and stabilizes intermediates with planar anthracene species. The potential driving force for experimentally observed antipodal bis-adduct is the gain in rotational entropy upon formation of complex **3**.

Given that in experiment only the formation of C_{60} and the antipodal bis-adduct occurs, despite the latter being the thermodynamically least stable of all C_{60}:anthracene bis-adducts, strongly suggests that crystal packing pre-aligns the structures to control the regiospecific reaction. These findings encourage new approaches of topochemically steered C_{60} multi-functionalization.

The intermediate structures **INT$_{Mono}$** and **INT$_{Bis}$** present a central point of interest, as they are to the best of our knowledge an unprecedented case of a perfectly planar molecule, trapped between equal and opposing π–π stacking interactions with 'curved' fullerenes. Our studies shed more light on the nature of π–π stacking interactions between a planar and (two) curved surfaces, as we report the first example of a double decker type of π–π stacking in an 'inverted sandwich' arrangement. These findings could open up new possibilities in designing functional fullerene based materials.

Author contributions

The manuscript was written through contributions of all authors. All authors have given approval to the final version of the manuscript.

Conflicts of interest

The authors declare no conflict of interest.

Funding sources

FWF (M-2005).

Acknowledgements

The computational results presented in this work have been achieved using the HPC infrastructure of the University of Innsbruck (leo3e) and the Vienna Scientific Cluster VSC3. M. P. would like to thank the Austrian Science Fund (FWF) for a generous Lise Meitner Fellowship (M-2005).

Notes and references

1 H. W. Kroto, J. R. Heath, S. C. Obrien, R. F. Curl and R. E. Smalley, *Nature*, 1985, **318**, 162–163.
2 H. W. Kroto, *Angew. Chem., Int. Ed. Engl.*, 1992, **31**, 111–129.
3 W. Krätschmer, L. D. Lamb, K. Fostiropoulos and D. R. Huffman, *Nature*, 1990, **347**, 354–358.
4 F. Wudl, *Acc. Chem. Res.*, 1992, **25**, 157–161.

5 F. Diederich and C. Thilgen, *Science*, 1996, **271**, 317–323.
6 J. M. Hawkins, *Acc. Chem. Res.*, 1992, **25**, 150–160.
7 H. Schwarz, *Angew. Chem., Int. Ed. Engl.*, 1992, **31**, 293–298.
8 A. Hirsch and M. Brettreich, *Fullerenes*, Wiley-VCH, Weinheim, 2005.
9 C. Bingel, *Chem. Ber.*, 1993, **126**, 1957–1959.
10 M. Prato and M. Maggini, *Acc. Chem. Res.*, 1998, **31**, 519–526.
11 Y. Garcia-Rodeja, M. Sola and I. Fernandez, *J. Org. Chem.*, 2018, **83**, 3285–3292.
12 I. Fernandez, M. Sola and F. M. Bickelhaupt, *Chem. – Eur. J.*, 2013, **19**, 7416–7422.
13 N. Villegas-Escobar, A. Poater, M. Sola, H. F. Schaefer and A. Toro-Labbe, *Phys. Chem. Chem. Phys.*, 2019, **21**, 5039–5048.
14 P. Belik, A. Gügel, J. Spickermann and K. Müllen, *Angew. Chem., Int. Ed. Engl.*, 1993, **32**, 78–80.
15 F. Diederich, U. Jonas, V. Gramlich, A. Herrmann, H. Ringsdorf and C. Thilgen, *Helv. Chim. Acta*, 1993, **76**, 2445–2453.
16 B. Kräutler and M. Puchberger, *Helv. Chim. Acta*, 1993, **76**, 1626–1631.
17 M. Tsuda, T. Ishida, T. Nogami, S. Kurono and M. Ohashi, *J. Chem. Soc., Chem. Commun.*, 1993, 1296–1298.
18 J. A. Schlüter, J. M. Seaman, S. Taha, H. Cohen, K. R. Lykke, H. H. Wang and J. M. Williams, *J. Chem. Soc., Chem. Commun.*, 1993, 972–974.
19 A. Duarte-Ruiz, T. Müller, K. Wurst and B. Kräutler, *Tetrahedron*, 2001, **57**, 3709–3714.
20 A. Duarte-Ruiz, K. Wurst and B. Kräutler, *Helv. Chim. Acta*, 2001, **84**, 2167–2177.
21 B. Kräutler, T. Müller and A. Duarte-Ruiz, *Chem. – Eur. J.*, 2001, **7**, 3223–3235.
22 F. Cataldo, D. A. Garcia-Hernandez and A. Manchado, *Fullerenes, Nanotubes, Carbon Nanostruct.*, 2015, **23**, 760–768.
23 F. Cataldo, D. A. Garcia-Hernandez and A. Manchado, *Fullerenes, Nanotubes, Carbon Nanostruct.*, 2015, **23**, 818–823.
24 G. H. Sarova and M. N. Berberan-Santos, *Chem. Phys. Lett.*, 2004, **397**, 402–407.
25 W. T. Su, M. Watanabe, Y. J. Chang, P. T. Chou, A. Ghosh and T. J. Chow, *Tetrahedron Lett.*, 2015, **56**, 1092–1095.
26 G.-W. Wang, Z.-X. Chen, Y. Murata and K. Komatsu, *Tetrahedron*, 2005, **61**, 4851–4856.
27 M. Sola, M. Duran and J. Mestres, *J. Am. Chem. Soc.*, 1996, **118**, 8920–8924.
28 S. Osuna and K. N. Houk, *Chem. – Eur. J.*, 2009, **15**, 13219–13231.
29 A. Chikama, H. Fueno and H. Fujimoto, *J. Phys. Chem.*, 1995, **99**, 8541–8549.
30 A. A. Peyghan and S. Yourdkhani, *Struct. Chem.*, 2014, **25**, 785–791.
31 M. Prato, *J. Mater. Chem.*, 1997, **7**, 1097–1109.
32 H. Wang, Q. W. Chen and S. Q. Zhou, *Chem. Soc. Rev.*, 2018, **47**, 4198–4232.
33 R. Macovez, *Front. Mater.*, 2018, **4**, 46.
34 C. C. Wang, Z. X. Guo, S. K. Fu, W. Wu and D. B. Zhu, *Prog. Polym. Sci.*, 2004, **29**, 1079–1141.
35 S. Collavini and J. L. Delgado, *Sustainable Energy Fuels*, 2018, **2**, 2480–2493.
36 C. J. Brabec, S. Gowrisanker, J. J. M. Halls, D. Laird, S. J. Jia and S. P. Williams, *Adv. Mater.*, 2010, **22**, 3839–3856.
37 G. V. Dubacheva, C. K. Liang and D. M. Bassani, *Coord. Chem. Rev.*, 2012, **256**, 2628–2639.
38 M. A. Faist, S. Shoaee, S. Tuladhar, G. F. A. Dibb, S. Foster, W. Gong, T. Kirchartz, D. D. C. Bradley, J. R. Durrant and J. Nelson, *Adv. Energy Mater.*, 2013, **3**, 744–752.
39 A. P. Proudian, M. B. Jaskot, C. Lyiza, D. R. Diercks, B. P. Gorman and J. D. Zimmerman, *Nano Lett.*, 2016, **16**, 6086–6091.
40 M. Rudolf, S. V. Kirner and D. M. Guldi, *Chem. Soc. Rev.*, 2016, **45**, 612–630.
41 I. Rasovic, *Mater. Sci. Technol.*, 2017, **33**, 777–794.
42 R. Bakry, R. M. Vallant, M. Najam-Ul-Haq, M. Rainer, Z. Szabo, C. W. Huck and G. K. Bonn, *Int. J. Nanomed.*, 2007, **2**, 639–649.
43 J. Lee, S. Mahendra and P. J. J. Alvarez, *ACS Nano*, 2010, **4**, 3580–3590.
44 A. M. Lopez, A. Mateo-Alonso and M. Prato, *J. Mater. Chem.*, 2011, **21**, 1305–1318.
45 D. Jariwala, V. K. Sangwan, L. J. Lauhon, T. J. Marks and M. C. Hersam, *Chem. Soc. Rev.*, 2013, **42**, 2824–2860.
46 L. K. Shrestha, Q. M. Ji, T. Mori, K. Miyazawa, Y. Yamauchi, J. P. Hill and K. Ariga, *Chem. – Asian J.*, 2013, **8**, 1662–1679.
47 V. Biju, *Chem. Soc. Rev.*, 2014, **43**, 744–764.
48 W. B. Yan, S. M. Seifermann, P. Pierrat and S. Brase, *Org. Biomol. Chem.*, 2015, **13**, 25–54.
49 J. Kotteritzsch, R. Geitner, J. Ahner, M. Abend, S. Zechel, J. Vitz, S. Hoeppener, B. Dietzek, M. Schmitt, J. Popp, U. S. Schubert and M. D. Hager, *J. Appl. Polym. Sci.*, 2018, **135**, 45916.
50 R. Geitner, J. Kotteritzsch, M. Siegmann, R. Fritzsch, T. W. Bocklitz, M. D. Hager, U. S. Schubert, S. Grafe, B. Dietzek, M. Schmitt and J. Popp, *Phys. Chem. Chem. Phys.*, 2016, **18**, 17973–17982.
51 A. Hirsch, I. Lamparth and H. R. Karfunkel, *Angew. Chem., Int. Ed. Engl.*, 1994, **33**, 437–438.
52 F. Djojo, A. Herzog, I. Lamparth, F. Hampel and A. Hirsch, *Chem. – Eur. J.*, 1996, **2**, 1537–1547.
53 J. F. Nierengarten, V. Gramlich, F. Cardullo and F. Diederich, *Angew. Chem., Int. Ed. Engl.*, 1996, **35**, 2101–2103.
54 A. Kraszewska, P. Rivera-Fuentes, G. Rapenne, J. Crassous, A. G. Petrovic, J. L. Alonso-Gomez, E. Huerta, F. Diederich and C. Thilgen, *Eur. J. Org. Chem.*, 2010, 4402–4411.
55 W. Y. Qian and Y. Rubin, *Angew. Chem., Int. Ed.*, 1999, **38**, 2356–2360.

56 W. Qian and Y. Rubin, *J. Am. Chem. Soc.*, 2000, **122**, 9564–9565.
57 R. Schwenninger, T. Müller and B. Kräutler, *J. Am. Chem. Soc.*, 1997, **119**, 9317–9318.
58 I. Lamparth, C. Maichle-Mössmer and A. Hirsch, *Angew. Chem., Int. Ed. Engl.*, 1995, **34**, 1607–1609.
59 A. Hirsch, I. Lamparth, T. Grösser and H. R. Karfunkel, *J. Am. Chem. Soc.*, 1994, **116**, 9385–9386.
60 F. Cardullo, L. Isaacs, F. Diederich, J. P. Gisselbrecht, C. Boudon and M. Gross, *Chem. Commun.*, 1996, 797–799.
61 G. Schick, M. Levitus, L. Kvetko, B. A. Johnson, I. Lamparth, R. Lunkwitz, B. Ma, S. I. Khan, M. A. Garcia-Garibay and Y. Rubin, *J. Am. Chem. Soc.*, 1999, **121**, 3246–3247.
62 B. Kräutler and J. Maynollo, *Angew. Chem., Int. Ed. Engl.*, 1995, **34**, 87–88.
63 A. Duarte-Ruiz, K. Wurst and B. Kräutler, *Helv. Chim. Acta*, 2008, **91**, 1401–1408.
64 F. Cataldo, D. A. Garcia-Hernandez and A. Manchado, *Fullerenes, Nanotubes, Carbon Nanostruct.*, 2014, **22**, 565–574.
65 B. Kräutler, T. Müller, J. Maynollo, K. Gruber, C. Kratky, P. Ochsenbein, D. Schwarzenbach and H. B. Burgi, *Angew. Chem., Int. Ed. Engl.*, 1996, **35**, 1204–1206.
66 A. Duarte-Ruiz, K. Wurst and B. Kräutler, *Helv. Chim. Acta*, 2001, **84**, 2167–2177.
67 A. Duarte-Ruiz, T. Müller, K. Wurst and B. Kräutler, *Tetrahedron*, 2001, **57**, 3709–3714.
68 W. Jia and G. P. Miller, *Fullerenes, Nanotubes, Carbon Nanostruct.*, 2008, **16**, 58–65.
69 A. Duarte-Ruiz, L. Echegoyen, A. Aya and F. Gomez-Baquero, *J. Mex. Chem. Soc.*, 2009, **53**, 169–173.
70 D. S. Sabirov, A. O. Terentyev and F. Cataldo, *Comput. Theor. Chem.*, 2016, **1081**, 44–48.
71 I. Fleming, in *Molecular Orbitals and Organic Chemical Reactions*, John Wiley & Sons Chichester, UK, 2010, pp. 253–368, DOI: 10.1002/9780470689493.ch6.
72 A. H. Streitwieser, C. Heathcock and E. M. Kosower, *Introduction to organic chemistry*, Macmillan, New York, 1992.
73 T. H. Lowry and K. S. Richardson, *Mechanism and Theory in Organic Chemistry*, Harper & Row, New York, 1976.
74 R. B. Woodward and R. Hoffmann, *Angew. Chem., Int. Ed. Engl.*, 1969, **8**, 781–853.
75 J. Sauer and R. Sustmann, *Angew. Chem., Int. Ed.*, 1980, **19**, 779–807.
76 M. B. Smith and J. March, *March's Advanced Organic Chemistry*, Wiley-Interscience, Hoboken New Jersey, 6th edn, 2007.
77 K. N. Houk, *J. Am. Chem. Soc.*, 1973, **95**, 4092–4094.
78 K. N. Houk, Y. Li and J. D. Evanseck, *Angew. Chem., Int. Ed. Engl.*, 1992, **31**, 682–708.
79 S. Osuna, M. Swart and M. Sola, *Phys. Chem. Chem. Phys.*, 2011, **13**, 3585–3603.
80 I. Lamparth, C. Maichlemossmer and A. Hirsch, *Angew. Chem., Int. Ed. Engl.*, 1995, **34**, 1607–1609.
81 G. W. Wang, M. Saunders and R. J. Cross, *J. Am. Chem. Soc.*, 2001, **123**, 256–259.
82 G. W. Wang, Z. X. Chen, Y. Murata and K. Komatsu, *Tetrahedron*, 2005, **61**, 4851–4856.
83 M. A. Herranz, N. Martin, J. Ramey and D. M. Guldi, *Chem. Commun.*, 2002, 2968–2969.
84 Y. Takaguchi, T. Tajima, K. Ohta, J. Motoyoshiya, H. Aoyama, T. Wakahara, T. Akasaka, M. Fujitsuka and O. Ito, *Angew. Chem., Int. Ed.*, 2002, **41**, 817–819.
85 K. N. Houk, Y. T. Lin and F. K. Brown, *J. Am. Chem. Soc.*, 1986, **108**, 554–556.
86 H. J. Jiao and P. V. Schleyer, *J. Phys. Org. Chem.*, 1998, **11**, 655–662.
87 E. Goldstein, B. Beno and K. N. Houk, *J. Am. Chem. Soc.*, 1996, **118**, 6036–6043.
88 K. N. Houk, J. Gonzalez and Y. Li, *Acc. Chem. Res.*, 1995, **28**, 81–90.
89 Y. Li and K. N. Houk, *J. Am. Chem. Soc.*, 1993, **115**, 7478–7485.
90 K. N. Houk, *Acc. Chem. Res.*, 1975, **8**, 361–369.
91 R. C. Haddon, *J. Am. Chem. Soc.*, 1997, **119**, 1797–1798.
92 R. C. Haddon, *Science*, 1993, **261**, 1545–1550.
93 F. M. Bickelhaupt and K. N. Houk, *Angew. Chem., Int. Ed.*, 2017, **56**, 10070–10086.
94 B. Willocq, V. Lemaur, M. El Garah, A. Ciesielski, P. Samori, J. M. Raquez, P. Dubois and J. Cornil, *Chem. Commun.*, 2016, **52**, 7608–7611.
95 S. Osuna, M. Swart and M. Sola, *J. Phys. Chem. A*, 2011, **115**, 3491–3496.
96 F. Diederich and R. Kessinger, *Acc. Chem. Res.*, 1999, **32**, 537–545.
97 Y. Nakamura, K. O-kawa and J. Nishimura, *Bull. Chem. Soc. Jpn.*, 2003, **76**, 865–882.
98 L. Chaker, A. B. Yongye, A. Nefzi and K. Martinez-Mayorga, *J. Phys. Org. Chem.*, 2012, **25**, 894–901.
99 M. Garcia-Borras, S. Osuna, M. Swart, J. M. Luis and M. Sola, *Chem. Commun.*, 2013, **49**, 1220–1222.
100 T. K. Roy Dennington and J. Millam, *GaussView 4.1.2*, Semichem Inc., Shawnee Mission, KS, 2009.
101 TURBOMOLE V7.3 2018, a development of University of Karlsruhe and Forschungszentrum Karlsruhe GmbH, 1989–2007, TURBOMOLE GmbH, since 2007; available from http://www.turbomole.com.
102 J. C. Slater, *Phys. Rev.*, 1951, **81**, 385–390.
103 S. H. Vosko, L. Wilk and M. Nusair, *Can. J. Phys.*, 1980, **58**, 1200–1211.
104 J. P. Perdew, *Phys. Rev. B: Condens. Matter Mater. Phys.*, 1986, **33**, 8822–8824.
105 A. D. Becke, *Phys. Rev. A*, 1988, **38**, 3098–3100.
106 A. Schäfer, H. Horn and R. Ahlrichs, *J. Chem. Phys.*, 1992, **97**, 2571–2577.
107 S. Grimme, J. Antony, S. Ehrlich and H. Krieg, *J. Chem. Phys.*, 2010, **132**, 154104.
108 A. Schäfer, C. Huber and R. Ahlrichs, *J. Chem. Phys.*, 1994, **100**, 5829–5835.

109 F. Weigend and R. Ahlrichs, *Phys. Chem. Chem. Phys.*, 2005, **7**, 3297–3305.
110 C. T. Lee, W. T. Yang and R. G. Parr, *Phys. Rev. B: Condens. Matter Mater. Phys.*, 1988, **37**, 785–789.
111 A. D. Becke, *J. Chem. Phys.*, 1993, **98**, 5648–5652.
112 P. C. Eklund, A. M. Rao, Y. Wang, P. Zhou, K. A. Wang, J. M. Holden, M. S. Dresselhaus and G. Dresselhaus, *Thin Solid Films*, 1995, **257**, 211–232.
113 A. P. Scott and L. Radom, *J. Phys. Chem.*, 1996, **100**, 16502–16513.
114 OriginPro, OriginLab Corporation, Version 2018b, 2018.
115 J. Contreras-Garcia, E. R. Johnson, S. Keinan, R. Chaudret, J. P. Piquemal, D. N. Beratan and W. T. Yang, *J. Chem. Theory Comput.*, 2011, **7**, 625–632.
116 E. R. Johnson, S. Keinan, P. Mori-Sanchez, J. Contreras-Garcia, A. J. Cohen and W. T. Yang, *J. Am. Chem. Soc.*, 2010, **132**, 6498–6506.
117 *The PyMOL Molecular Graphics System, Version 1.8*, Schrödinger, LLC, 2018.
118 W. Humphrey, A. Dalke and K. Schulten, *J. Mol. Graphics Modell.*, 1996, **14**, 33–38.
119 L. P. Wolters and F. M. Bickelhaupt, *Wiley Interdiscip. Rev.: Comput. Mol. Sci.*, 2015, **5**, 324–343.
120 D. H. Ess and K. N. Houk, *J. Am. Chem. Soc.*, 2007, **129**, 10646–10647.
121 S. E. Zhu, F. Li and G. W. Wang, *Chem. Soc. Rev.*, 2013, **42**, 7535–7570.
122 V. Neti, M. R. Ceron, A. Duarte-Ruiz, M. M. Olmstead, A. L. Balch and L. Echegoyen, *Chem. Commun.*, 2014, **50**, 10584–10587.
123 M. R. Ceron and L. Echegoyen, *J. Phys. Org. Chem.*, 2016, **29**, 613–619.
124 D. Sepulveda, Y. F. Guan, U. Rangel and S. E. Wheeler, *Org. Biomol. Chem.*, 2017, **15**, 6042–6049.
125 M. M. Li, Y. B. Wang, Y. Zhang and W. Wang, *J. Phys. Chem. A*, 2016, **120**, 5766–5772.
126 R. G. Huber, M. A. Margreiter, J. E. Fuchs, S. von Grafenstein, C. S. Tautermann, K. R. Liedl and T. Fox, *J. Chem. Inf. Model.*, 2014, **54**, 1371–1379.
127 J. W. Li, Y. Y. Liu, Y. Qian, L. Li, L. H. Xie, J. Z. Shang, T. Yu, M. D. Yi and W. Huang, *Phys. Chem. Chem. Phys.*, 2013, **15**, 12694–12701.